IEEE Access
Multidisciplinary | Rapid Review | Open Access Journal

Received July 14, 2019, accepted July 27, 2019, date of publication August 1, 2019, date of current version August 15, 2019.

Digital Object Identifier 10.1109/ACCESS.2019.2932387

A Polyetheretherketone Six-Axis Force/Torque Sensor

LIYUE FU, (Student Member, IEEE), AIGUO SONG, (Senior Member, IEEE), AND DAPENG CHEN, (Student Member, IEEE)

State Key Laboratory of Bioelectronics, Jiangsu Key Lab of Remote Measurement and Control, School of Instrument Science and Engineering, Southeast University, Nanjing 210096, China

Corresponding author: Aiguo Song (a.g.song@seu.edu.cn)

This work was supported in part by the National Key Research and Development Program of China under Grant 2016YFB1001301, and in part by the National Nature Science Foundation of China under Grant U1713210.

ABSTRACT At present, six-axis force/torque (F/T) sensor has been increasingly used in robot application, and most of the elastic elements of resistance strain type F/T sensors are made of metal materials, such as alloy steel, stainless steel, aluminum alloy, and so on. In this paper, a novel six-axis F/T sensor based on Polyetheretherketone (PEEK) material is presented. Comparison with ordinary F/T sensor purpose was served by building simplified statics model that demonstrates the conclusion of highly sensitivity of the F/T sensor based on PEEK material. The strain mapped on the strain sensitive path was analyzed using finite element analysis (FEA), frequency response curves were depicted by means of harmonic analysis, and the static and dynamic performances analyses of the six-axis F/T sensor based on PEEK material (later called PEEK sensor) were studied. Moreover, the properties of this sensor were compared with a six-axis F/T sensor based on aluminum alloy 2024 material (later called metallic sensor). The results show the properties of linearity ($\leq$1%), hysteresis ($\leq$2%), high sensitivity (force: $\geq 2.37\times10^{-4}$/N; torque (*Tx*, *Ty*): 0.19×10^{-4}/Nmm), and crosstalk ($\leq$8%) between the dominant F/T component and other components. The dynamic response time of the PEEK sensor was also measured via dynamic calibration experiment, which is much higher than that of the metallic sensor. This study demonstrates that the PEEK sensor has a comparable static performance with the metallic sensor, and even higher sensitivity, but it is only suitable for measurement below 200 Hz.

INDEX TERMS Six-axis force/torque sensor, polyetheretherketone (PEEK), response time, sensitivity.

I. INTRODUCTION

Force sensing systems have emerged in a variety of industrial automation equipment since the late 1970s [1]–[5]. The necessity of measuring all the six components of a generalized force is relevant in many activities, such as testing for wind tunnels [6], assembly operation of robotic arms [7]–[11], measuring a wheel hub [9]–[10], and so on. Especially in the field of robot, six-axis F/T sensor has been widely applied. It is well recognized that the acquisition of high-quality multi-axis F/T sensor signals during a physical interaction between a robot hand and an object can greatly improve the manipulation capability of the robot system [11]. Various types of six-axis F/T sensors with different structures have been developed by researchers. Song *et al.* [12] developed a self-decoupled 4 DOF F/T sensor with a cross elastic beam, and this sensor had low cross sensitivity without decoupling matrix. Guggenheim *et al.* [13] designed a robust and inexpensive six-axis F/T sensor using MEMS barometers, which can be assembled in two days with off-the-shelf components for less than 20 USD. A novel six-axis F/T sensor based on capacitive transduction principle was presented in [14]. The six-axis F/T sensor was performed by six capacitance sensor cells, which were designed by using both parallel and orthogonal arrangements of the two electrode plates. Zhang *et al.* [15] developed a novel T-shaped five-axis piezoresistive force/torque sensor, which has good linearity and low hysteresis, but very low measurement range. It is impossible to realize full isotropy in theory for the general 6-6 Stewart platform-based force sensor, hence a novel 6/3-3 Stewart platform-based sensor was proposed in 2008 by Yao *et al.* [16]. Zhao *et al.* [17] presented a large measurement range and high accuracy 6-UPUR six-axis

The associate editor coordinating the review of this manuscript and approving it for publication was Zhong-Ke Gao.

force sensor with flexible joints to overcome the influence of the gap and friction of the traditional joints on the parallel six-axis sensors' precision and stability. Liang *et al.* [18] designed a six-axis wrist F/T sensor based on E-shape membranes and compared it with a cross-beam sensor, and the results showed that maximum interference error and nonlinearity error are 1.6% F.S. and 0.17% F.S., respectively.

Most of traditional industrial robots use position control and planning to achieve the desired trajectory. According to the external contact force, adjust the relative position of shaft and hole, comply with the assembly fit force, reduce the assembly error, and finally realize the assembly operation. Compared to passive compliance with spring mechanism, active compliance doesn't change the rigidity of robot, and the range and precision of compliance are greatly improved. The common practice of active compliance is to install multi-axis F/T sensor at the end of the robot, and realize compliance control task by means of force feedback and control algorithm [19], [20]. When the end-load of robot is small, in order to ensure the precision of force control, the multi-axis F/T sensor with small range and high sensitivity is needed.

At present, most of the elastic elements of resistance strain type F/T sensors are made of metal materials, such as alloy steel, stainless steel, aluminum alloy and so on. The sensor of aluminum alloy has been widely used in the field of small range owing to its light weight, high accuracy, and so forth. With regard to the six-axis F/T sensor with metal strain gages, the sensitivity is related to the structure and size of its elastic element. For a six-axis F/T sensor with cross-beam structure, the thinner the cross beam, the higher the sensitivity. However, too thin cross beam is not conductive to strain gauge adhesion. Consequently, it is necessary to find a more sensitive material for making elastic element, and some mechanical properties of this material should also meet the corresponding requirements.

PEEK is a macromolecule polymer, which was first synthesized by ICI (Imperial Chemical Industry) Company in England in 1964. With good toughness and rigidity, it is the most perfect material for combination of toughness and rigidity in all resins [21]. It has excellent fatigue resistance to alternating stress compared to alloy materials, and also good insulation and electrical properties. Therefore we select PEEK material as a substitute for aluminum alloy 2024 to make cross-beam elastic element. In order to show the performances of the six-axis F/T sensor made of PEEK material better, two F/T sensors prototypes with identical structures and sizes, but different materials (i.e. PEEK and Aluminum alloy 2024) of the cross-beam elastic element are made. The calibration experiments of the two F/T sensors are conducted, and the performances of the two sensors are compared.

In this paper, a six-axis F/T sensor based on PEEK material (PEEK sensor) is developed. Firstly, the maximum strain on the strain gauge paste path and frequency response characteristics are obtained by means of finite element analysis (FEA). Secondly, static calibration experiment is carried out to acquire static performance indices, such as linearity, repeatability, hysteresis, sensitivity, crosstalk and so forth. Lastly, the dynamic response time of the PEEK sensor is gained by step-response method in the dynamic calibration test. Almost all of the test results aforementioned are compared with those of the F/T sensor made of aluminum alloy 2024 material (metallic sensor). The comparison results show that the PEEK sensor has a comparable static performance with the metallic sensor, and the sensitivity is tens of times that of the metallic sensor. This provides a theoretical basis for the design of high sensitivity multi-axis F/T sensors.

II. DESCRIPTION OF THE F/T SENSORS

As shown in Fig. 1a, the prototype of the six-axis wrist F/T sensor consists of four parts: pedestal, cross-beam elastic element (elastic beam), top cover and calibration pillar. Elastic beam is the core component of the sensor, and the performance of the sensor mainly relies on it. Compared with other mechanical structures, cross-beam structure has obvious advantages [22], such as high symmetry, compact structure, large rigidity, easy to machine, etc. So cross-beam structure is selected as structure of the elastic element of the

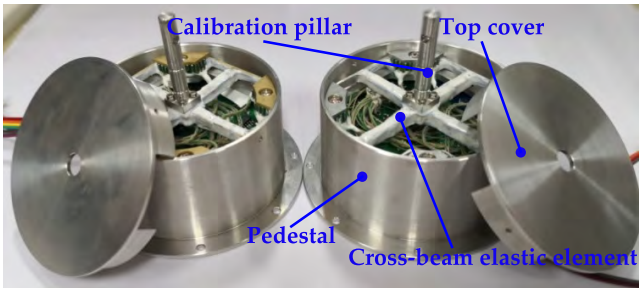

(a)

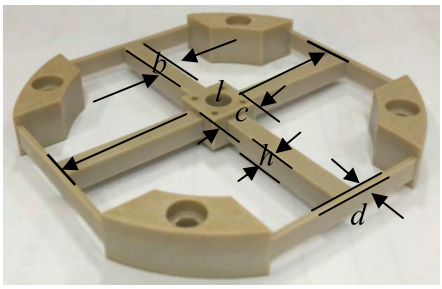

(b)

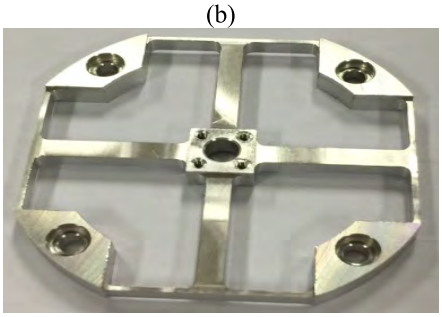

(c)

FIGURE 1. (a) Prototypes of the two six-axis F/T sensors: Left—the PEEK sensor, right—the metallic sensor; (b) The elastic beam made of PEEK; (c) The elastic beam made of aluminum alloy 2024.

six-axis writst F/T sensor. Calibration pillar is required to convert an applied force into a distributed stress in the elastic beam. When a force is applied on the calibration pillar, it is decoupled into six components: three force terms along x-, y-, z-axis (*Fx*, *Fy*, *Fz*) and three torque terms around x-, y-, z-axis (*Tx*, *Ty*, *Tz*). Six independent Wheatstone bridges are used to measure the sensor output. Fig. 1a also shows two six-axis F/T sensors with identical structures and sizes, but different materials of the elastic beams: one is of PEEK material, and the other is of aluminum alloy 2024, as shown in Fig. 1b, 1c, respectively. Parameters of the elastic beam are shown in Table 1, where b, h and l denote the width, height and length of the cross beam, respectively, d represents the thickness of the compliant beam, and c represents the width of central platform of cross-beam elastic element.

TABLE 1. Parameters of the cross-beam.

Parameter	Value
b /mm	3.8
h /mm	3.8
l /mm	64
d /mm	1
c /mm	10

Comparison of mechanical properties between PEEK [23]–[27] and aluminum alloy 2024 [28] is shown in Table 2.

TABLE 2. Typical mechanical properties of PEEK and aluminum alloy 2024.

items	PEEK	2024
yield strength /MPa	97	325
yield strain	3.5%	0.45%
elasticity modulus /GPa	2.8	72
linear expansivity /10^{-5}K^{-1} (10~180℃)	4.8	2.3
Heat deformation temperature /℃ (1.82MPa)	152	--
density / kg/m^3	1320	2780

III. SIMPLIFIED STATICS MODEL

The elastic beam of the F/T sensor is a hyperstatic structure. The cross beams have bending deformation when forces/torques in different directions are applied on the central position of the elastic element. Deflection characteristics of the flexural beams are analyzed by Timoshenko beam theory [29], [30]. The deformation of the elastic beam can be expressed by the deflection (ω) and rotation angle (φ) of a point on this beam, as is depicted in (1). An infinitesimal section of a Timoshenko beam is illustrated in Fig. 2.

$$\begin{cases} M(x) = -EI\dfrac{d\varphi(x)}{dx} \\ F_Q(x) = kGA(\dfrac{d\omega(x)}{dx} - \varphi(x)) \end{cases} \tag{1}$$

where M is the bending moment and F_Q is the shear force, A denotes the cross-sectional area, E, G, I, k are the elastic modulus, shear modulus, moment of inertia, and shear coefficient, respectively.

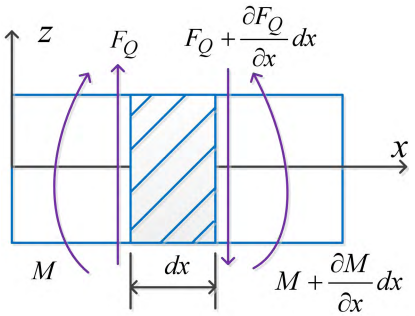

FIGURE 2. A Timoshenko beam and its infinitesimal section.

Based on (1) and Fig. 2, equation (2) can be yielded:

$$\begin{cases} \dfrac{d}{dx}\left[kGA\left(\dfrac{d\omega(x)}{dx} - \varphi(x)\right)\right] = 0 \\ \dfrac{d}{dx}\left[EI\dfrac{d\varphi(x)}{dx} - kGA\left(\dfrac{d\omega(x)}{dx} - \varphi(x)\right)\right] = 0 \end{cases} \tag{2}$$

Equations (1) and (2) are two basic formulas of Timoshenko beam theory. Analytical solutions of $\omega(x)$ and $\varphi(x)$ can be obtained from the above equations when given enough boundary conditions. And then the strain value [31] of any point in the cross beam can be calculated in (3) as follows:

$$\varepsilon(x, z) = -z\frac{d\varphi(x)}{dx} \tag{3}$$

where z is the distance between the point and the neural plane.

As shown in Fig. 3a, when Fx is loaded, bending deformation occurs on the principal beams PQ, RS and compliant beams EF, GH. Compliant beams JK and MN are considered as the roller support of the principal beams PQ and RS. We can ignore the small central platform when analyzing the bending deformation of elastic beams. Moreover, the principal beams PQ and RS can be regarded as beam PS. Bending deformation of the principal beam PS is illustrated in Fig. 3d. The shear force and bending moment on an arbitrary section of the beam are as follows:

$$F_Q = \begin{cases} F/2, & 0 \le x \le l/2 \\ -F/2, & l/2 < x \le l \end{cases} \tag{4}$$

$$M(x) = \begin{cases} Fx/2, & 0 \le x \le l/2 \\ F(l-x)/2, & l/2 < x \le l \end{cases} \tag{5}$$

Equations (6) and (7) can be deduced by the simultaneous equations (1), (2), (4), (5). It should be noted that the following equations are valid under the condition $0 \le x \le l/2$.

$$kGA\left[\frac{d\omega(x)}{dx} - \varphi(x)\right] = \frac{F}{2} \tag{6}$$

$$\frac{d}{dx}\left[EI\frac{d\varphi(x)}{dx}\right] = \frac{F}{2} \tag{7}$$

Based on the differential equation of the deflection and the above equations, the deflection and rotation angle of a point

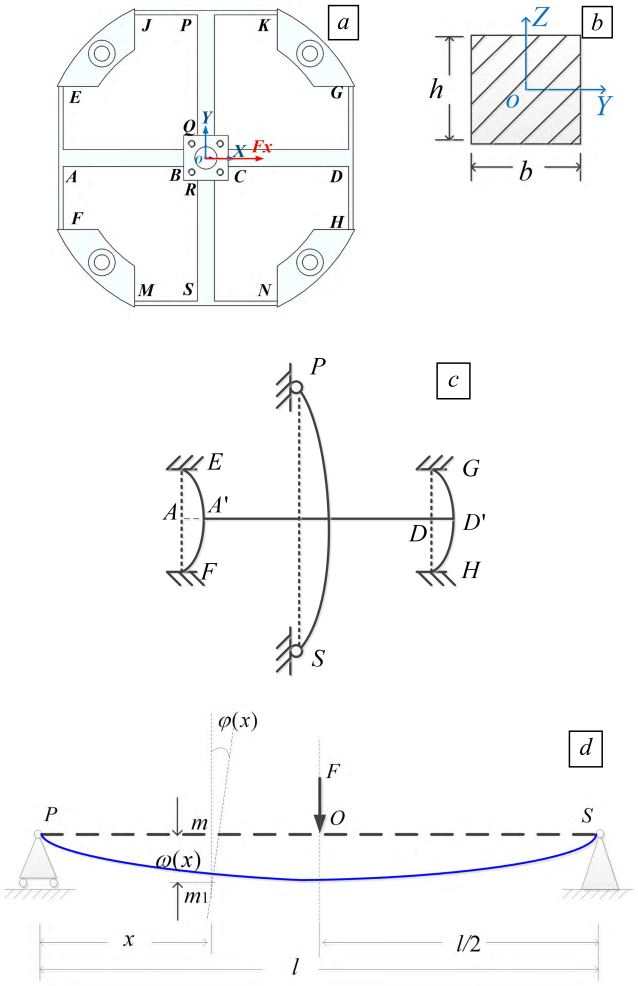

FIGURE 3. The cross-beam elastic body of the F/T sensor: (a) the schematic diagram of the elastic beam; (b) cross section of the principal beam; (c) mechanical model of an elastic body under *Fx*; (d) bending deformation of the beam *PS* under force.

on the principal beam are derived [32]:

$$\begin{cases} \omega(x) = -\dfrac{Fl^2x}{16EI} + \dfrac{Fx^3}{12EI} - \dfrac{Fx}{2kGA} \\ \varphi(x) = -\dfrac{Fl^2}{16EI} + \dfrac{Fx^2}{4EI} - \dfrac{F}{2kGA} \end{cases} \tag{8}$$

By substituting (8) to (3), the strain value on the principal beam can be deduced as follows:

$$\varepsilon(x, z) = \frac{Fxz}{2EI} \tag{9}$$

Cross section of the principal beam PS is depicted in Fig. 3b, from which moment of inertia I of this section can be obtained: $I = b^3h/12$. And then the strain at the central point of the principal beam surface ($x = l/2, z = h/2$) is

$$\varepsilon = \frac{3Fl}{2Eb^3} \tag{10}$$

It is shown from (10) that the strain on the surface of the cross beam depends not only on the size of beam and the applied force, but also on elastic modulus of the beam's material. Based on table 1 and 2, the strain at the central point of the principal beam under force Fx can be obtained as follows:

$$\begin{cases} \boldsymbol{\varepsilon}_{10} = 2.43 \times 10^{-3} \\ \boldsymbol{\varepsilon}_{20} = 9.37 \times 10^{-3} \end{cases} \tag{11}$$

where ε_{10} is strain of the elastic beam based on aluminum alloy material under $Fx = 200$N (full range of the metallic sensor), and ε_{20} is strain of the elastic beam based on PEEK material under $Fx = 30$N (full range of the PEEK sensor).

Strain gages are usually pasted on the surface of the principal beam about $\Delta = 3mm$ from the central platform, and thus we should calculate the strain value in this location ($x = (l - c)/2 - \Delta$). The strains of the principal beams of two materials (*i.e.* aluminum alloy and PEEK) can be derived as follows.

$$\begin{cases} \boldsymbol{\varepsilon}_1 = 1.82 \times 10^{-3} \\ \boldsymbol{\varepsilon}_2 = 7.02 \times 10^{-3} \end{cases} \tag{12}$$

Obviously, the sensitivity of the elastic beam based on PEEK material is 26 times of the beam based on aluminum alloy material.

IV. FINITE ELEMENT ANALYSIS

The stress analysis of elastic beam is carried out in FEA software – ANSYS. The deformation of the elastic beam is shown in Fig. 4a when the force is applied along x-axis. Select a straight path from the central platform to the compliant beam, as shown in the red line segment in Fig. 4a, on the centerline of the bending beam's surface. The strain of each node on the path is analyzed in all directions. When the elastic beam is subjected to load in Fx direction, the strain distributions on the path of the PEEK sensor and the metallic sensor are shown in Fig. 4b, 4c respectively. As can be seen from this Figure, except for the two ends of the cross beam, the strains distribution on the cross beam vary linearly, and the strain near the center is the largest. The maximum strain on the path is 5.243×10^{-3} when the force Fx is 30 N for the PEEK elastic beam; whereas the maximum strain is 1.296×10^{-3} when Fx is 200 N for the metallic elastic beam. And hence the sensitivity of PEEK is 26 times of aluminum alloy 2024 in Fx direction. Likewise, the maximum strain analyses on the path of the two elastic beams in other directions are shown in Table 3.

Furthermore, the natural frequencies and modes of elastic beams are obtained by modal analysis, as shown in Table 4 and Fig. 5. As illustrated in Table 4, the natural frequencies of the metallic sensor are about 3.5 times that of the PEEK sensor. Since multi-dimensional F/T sensor is a low pass sensor, we can take the natural frequency of 1/3 as its working bandwidth. Then the working bandwidth of the PEEK sensor and the metallic sensor are 190Hz, 660Hz, respectively.

Similarly, frequency response curves of elastic beams are depicted by harmonic analysis in Fig. 6. It can be seen from

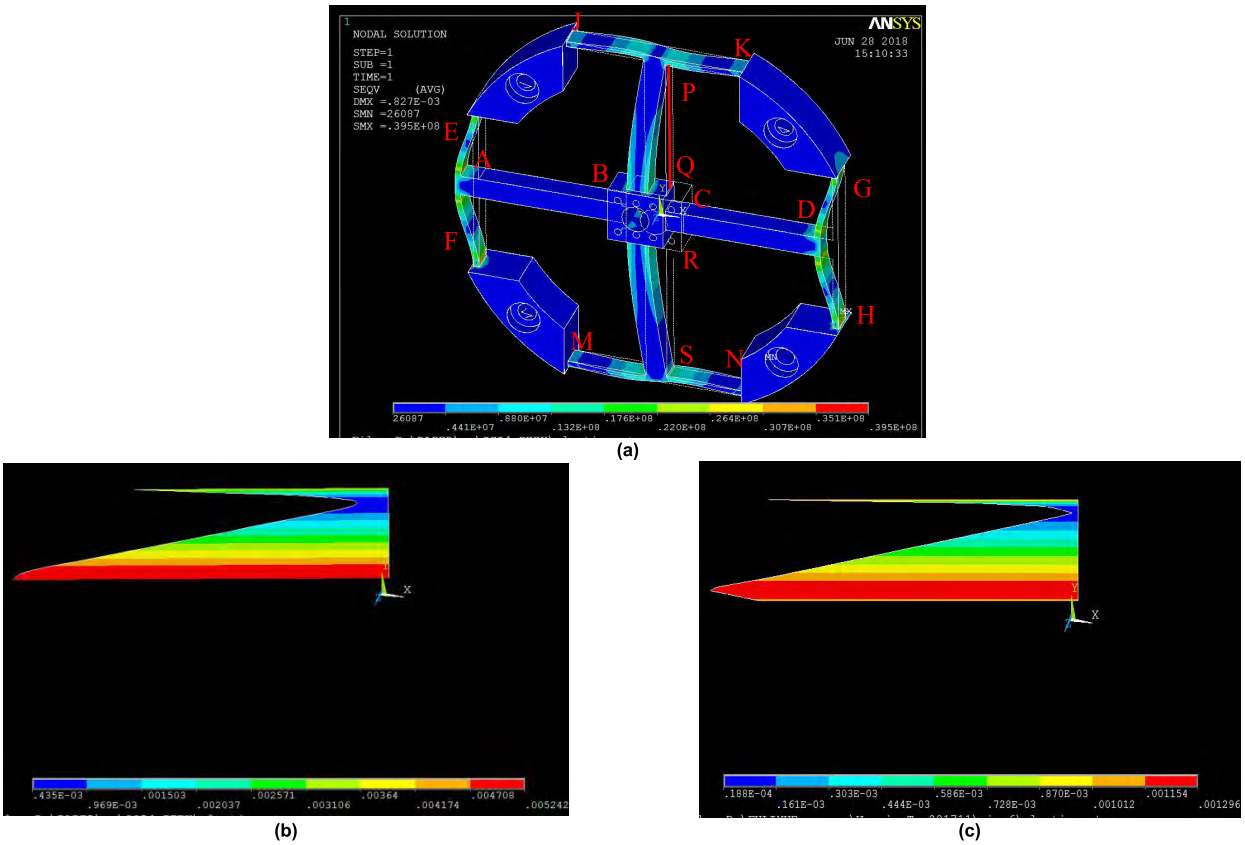

FIGURE 4. The stress/strain distributions when load is imposed in *Fx* direction: (a) the deformation of the cross beams; (b) the strain distribution on the path of the PEEK elastic beam; (c) the strain distribution on the path of the metallic elastic beam.

TABLE 3. The maximum strain mapped on the path.

Load	Fx		Fz		Tx		Tz	
	30 N (PEEK)	200 N (metallic)	30 N (PEEK)	200 N (metallic)	300 Nmm (PEEK)	2000 Nmm (metallic)	500 Nmm (PEEK)	4000 Nmm (metallic)
Strain /10^{-3}	5.243	1.296	7.159	1.855	3.987	1.017	3.752	1.128

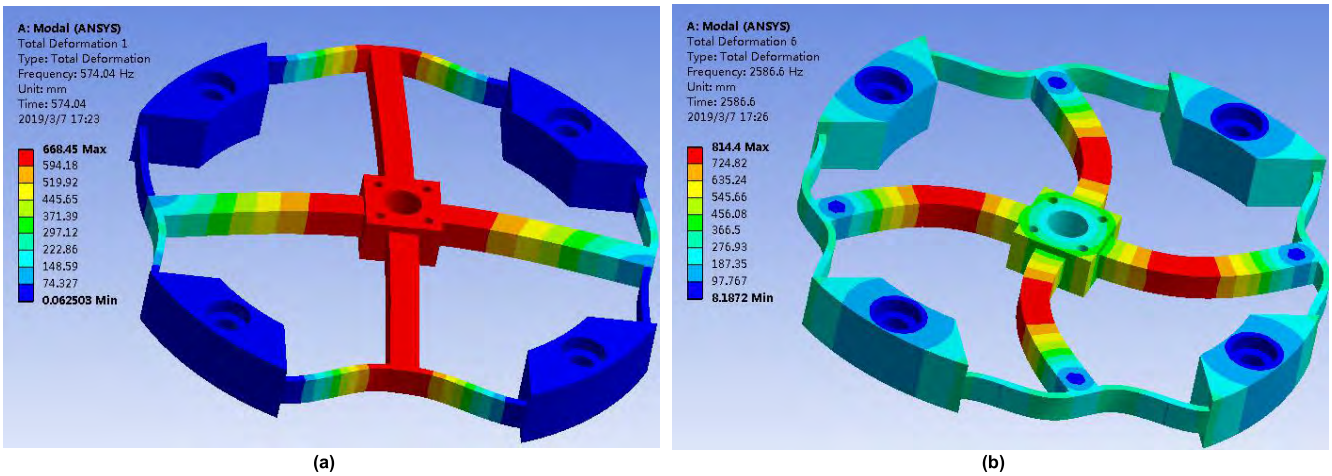

FIGURE 5. (a)The first order vibration mode—translation along X-axis; (b)The six order vibration mode—rotation around Z-axis.

the Figure that the frequencies at the peak amplitude are 571Hz, 1981.8Hz respectively, which are basically coincident with the conclusion given in Table 4.

V. STATIC PERFORMANCES ANALYSIS AND DISCUSSION

In this section, static calibration experiments are designed and performed to obtain static performances of the

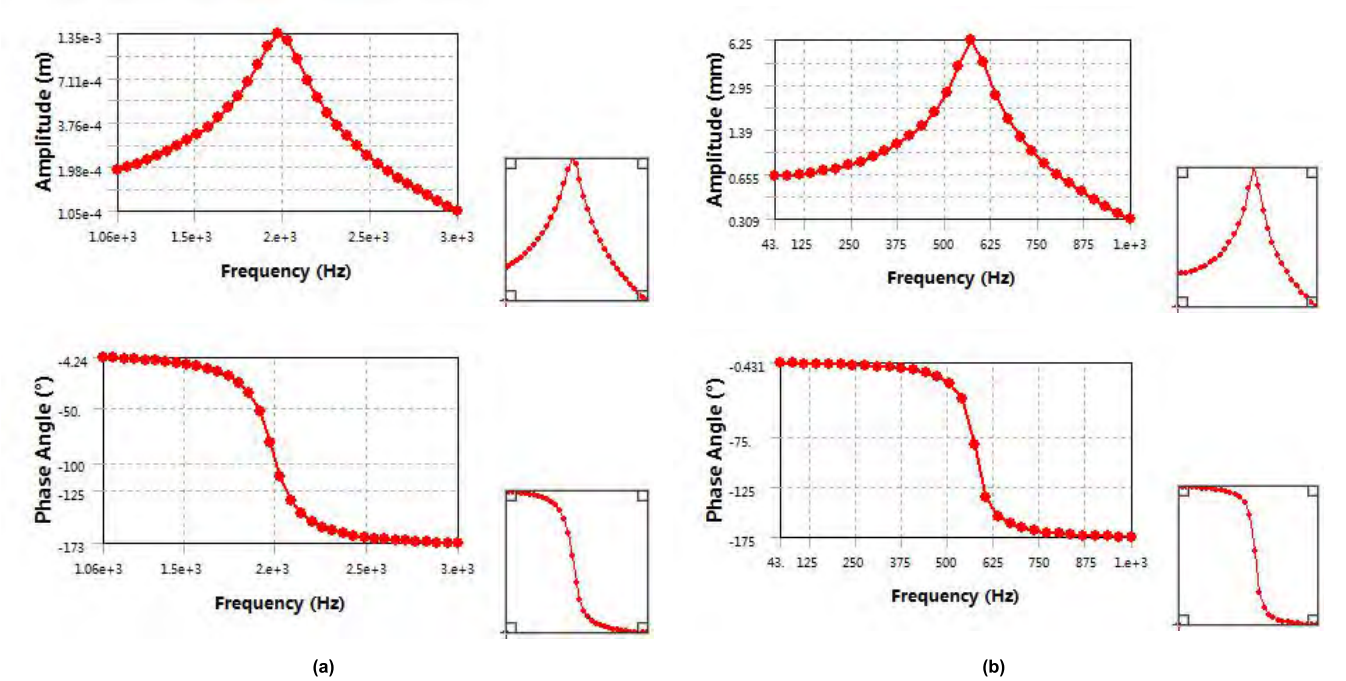

FIGURE 6. The frequency response curves of the two sensors: (a) the metallic sensor; (b) the PEEK sensor.

TABLE 4. The first six natural frequencies and modes.

Order	Frequency /Hz		Vibration Mode
	PEEK	metallic	
1	574	1982.8	Translation along X-axis
2	574.6	1983.2	Translation along Y-axis
3	600.3	2085.2	Translation along Z-axis
4	1876.2	6532.3	Rotation around X-axis
5	1876.8	6533.5	Rotation around Y-axis
6	2586.6	8979.1	Rotation around Z-axis

two six-axis F/T sensors (PEEK sensor and metallic sensor). The calibration experimental device is shown in Fig. 7. The device mainly includes indexing plate and several pulleys.

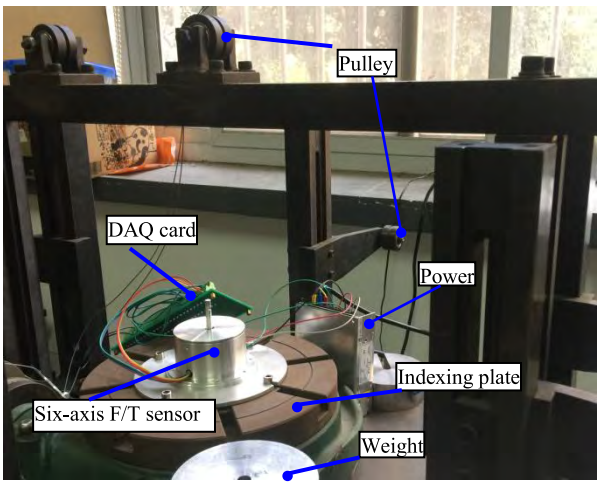

FIGURE 7. The calibration experimental device.

The F/T sensor is mounted on a rotatable indexing plate to guarantee directions of loading forces and torques, and a set of standard test weights are attached on the calibration pillar through a pulley. Thus, the gravity of weights corresponded to the loading forces or torques on the sensor. Pulleys around the indexing plate are used to calibrate torques around x, y, and z axis, and forces along x, y axis; whereas pulleys above the indexing plate are used to calibrate the force along z axis. The output voltages of Wheatstone bridges are amplified and acquired by DAQ card—NET2801. In calibration experiments, only one-dimensional force is applied each time, while the output voltages of all directions are recorded simultaneously. After obtaining the calibration test data, static performance indices such as linearity, repeatability, hysteresis, and sensitivity are achieved by static analysis.

Fig. 8 illustrates the calibration test curves of the two sensors due to the applied forces or torques. These curves depict relative variation of strain gauge resistance versus the applied forces or torques. It is obvious from the figure that the PEEK sensor outputs vary linearly with the applied force. By analyzing the calibration test data, the performances of the PEEK sensor, such as linearity, repeatability, hysteresis, sensitivity, and so on, are investigated.

A. LINEARITY

The linearity of a six-axis F/T sensor is the degree to which the input-output relation curve in the same direction deviates from a straight line, and usually expressed as nonlinearity error. Linear fitting equations and nonlinearity errors in each direction of the two F/T sensors are achieved by means of the least square linear fitting method, as shown in Table 5. R^2 is

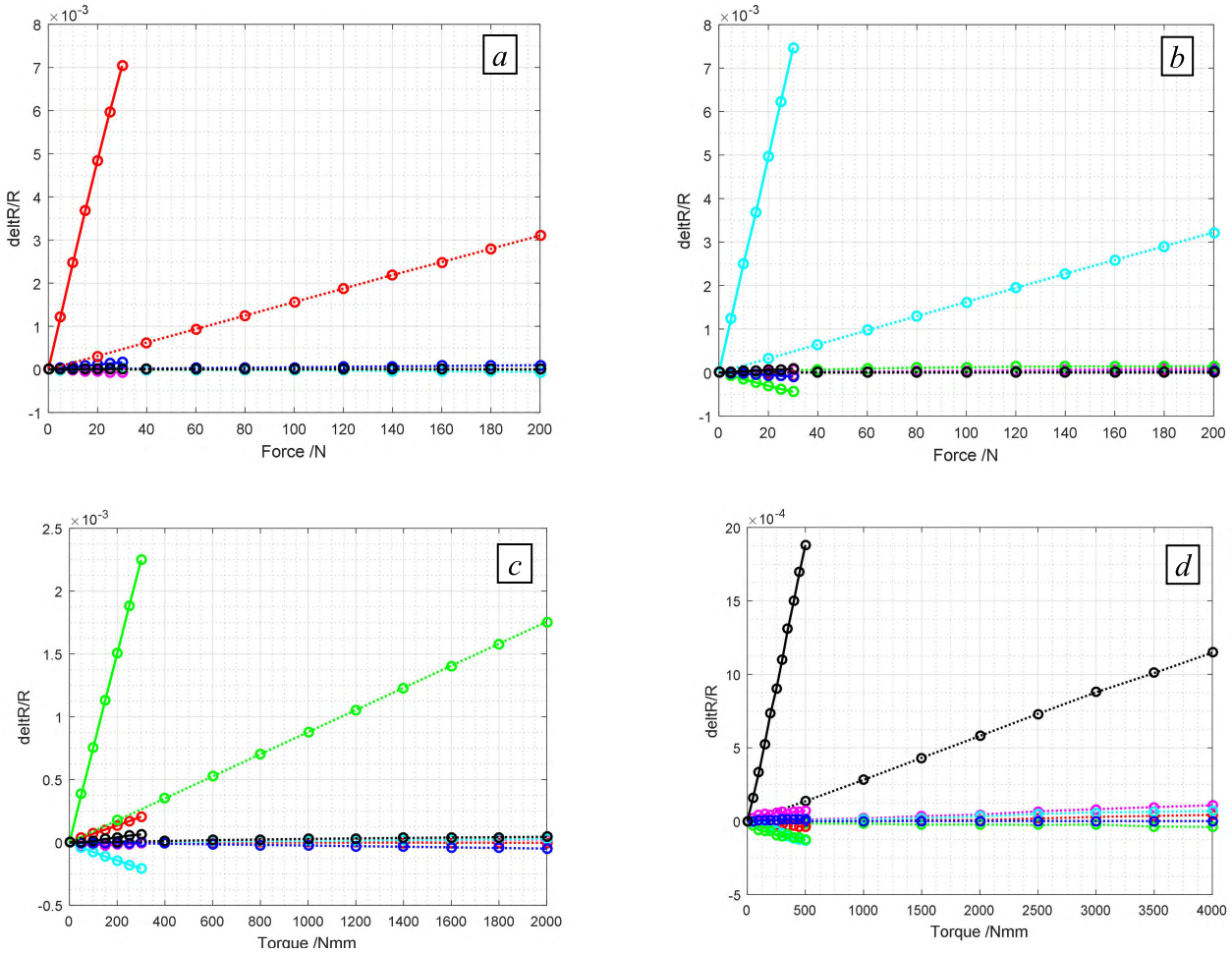

FIGURE 8. Calibration test curves of the two sensors due to the applied forces or torques (full lines—PEEK sensor, dotted lines—metallic sensor).

TABLE 5. The linearity in each channel of the two F/T sensors.

channel	PEEK sensor			metallic sensor		
	Linear fitting equation	R^2	Nonlinearity error	Linear fitting equation	R^2	Nonlinearity error
Fx	Y=0.2837x+0.3920	0.9912	⩽1% F.S.	Y=0.0456x+0.0353	0.9989	⩽0.5% F.S.
Fy	Y=0.3021x-0.3314	0.9908	⩽1% F.S.	Y=0.0471x-0.1081	0.9979	⩽0.5% F.S.
Fz	Y=0.3222x-0.5194	0.9956	⩽0.5% F.S.	Y=0.0472x-0.0993	0.9986	⩽0.5% F.S.
Tx	Y=30.81x-0.0521	0.9986	⩽0.5% F.S.	Y=4.01x+0.2754	0.9989	⩽0.5% F.S.
Ty	Y=30.92x-0.4913	0.9979	⩽0.5% F.S.	Y=4.09x-0.5203	0.9992	⩽0.5% F.S.
Tz	Y=17.1x+0.7682	0.9902	⩽1% F.S.	Y=1.403x+0.4329	0.9941	⩽1% F.S.

square of correlation coefficient between the linear fitting equation and original data points. The linear fitting in several channels is depicted in Fig. 8. Results from these diagrams reflect that although the linearity of the F/T sensor made of aluminum alloy is better, the nonlinearity error of PEEK sensor is basically less than 1%, which meets the general requirements.

B. REPEATABILITY

The repeatability of a six-axis F/T sensor can be expressed as non-repeatability error. In the static calibration test, the two F/T sensors are loaded and unloaded three times in each channel. The input-output relation curves in *Fx* channel are shown in Fig. 9, and the non-repeatability errors are 1.53%, 1.96% respectively. The comparisons of repeatability characterization of the two F/T sensors are depicted in Table 6. As can be seen in the table, except for *Tz* channel, the non-repeatability errors of the PEEK sensor are about the same as that of the metallic sensor, which are less than 2%. The reason for the large non-repeatability error in *Tz* channel is mainly due to screw fastening between the calibration cap used in *Tz* channel and the calibration pillar. Under the influence of

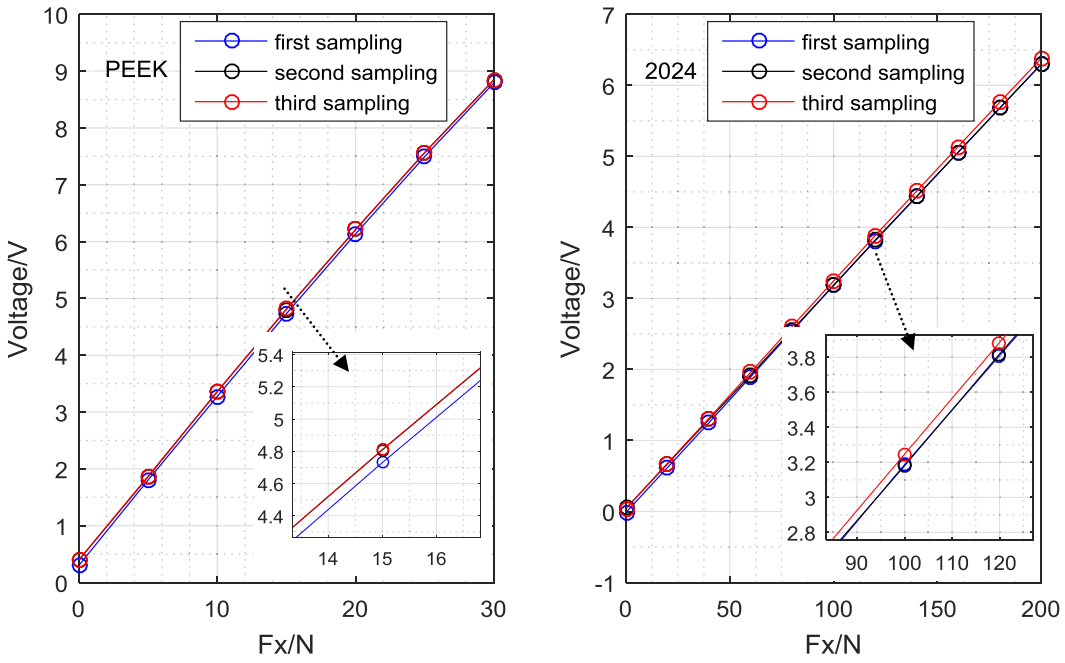

FIGURE 9. The comparison of repeatability curves of the two F/T sensors in *Fx* channel.

TABLE 6. The non-repeatability errors in each channel of the two F/T sensors.

channel	PEEK sensor /%F.S.	metallic sensor /%F.S.
Fx	±1.53	±1.96
Fy	±1.85	±1.92
Fz	±1.29	±0.41
Tx	±1.06	±1.35
Ty	±1.13	±0.88
Tz	±2.21	±1.5

machining precision, there is relative rotation between the cap and the pillar, which results in the difference of the arm of force during the forward and reverse stroke.

C. HYSTERESIS

Hysteresis characteristics can indicate the degree of inconsistency between the input-output characteristics curves during the forward and reverse stroke of the sensor, and it is usually represented by hysteresis error. The hysteresis curves of PEEK sensor obtained when force (*Fx*, *Fy*, *Fz*) is increasing from 0 to 30N, and decreasing back to 0N, are shown in Fig. 10a; whereas Fig. 10b illustrates the hysteresis curves of the metallic sensor. All the measurements are repeated three times under the same experimental conditions. The comparisons of hysteresis characterization of the two F/T sensors are depicted in Table 7. It can be shown from this table that the maximum hysteresis error is 1.99% (*Tz* channel), which is not a significant deviation for the application.

D. SENSITIVITY

The slopes of the curves in Fig. 8 represent the strain sensitivities of the sensor, which are listed in Table 8. It can be

TABLE 7. The hysteresis errors comparison between the PEEK sensor and the metallic sensor.

channel	PEEK sensor /%F.S.	metallic sensor /%F.S.
Fx	±1.75	±1.97
Fy	±1.88	±1.26
Fz	±1.33	±0.56
Tx	±1.2	±0.59
Ty	±1.31	±0.62
Tz	±1.92	±1.99

TABLE 8. The strain sensitivity in each channel of the two F/T sensors.

channel	PEEK sensor	metallic sensor
Fx /$\times 10^{-4}$/N	2.37	0.11
Fy /$\times 10^{-4}$/N	2.46	0.11
Fz /$\times 10^{-4}$/N	2.5	0.17
Tx /$\times 10^{-4}$/Nmm	0.19	0.013
Ty /$\times 10^{-4}$/Nmm	0.19	0.013
Tz /$\times 10^{-4}$/Nmm	0.038	0.00295

seen from the table that the strain sensitivities of the PEEK sensor are 21.55, 22.36, 14.7, 14.6, 14.6, and 12.9 times that of the metallic sensor in *Fx*, *Fy*, *Fz*, *Tx*, *Ty*, and *Tz* channels, respectively. The difference in sensitivity between *Fx* and *Fy* channel is mainly due to adhesion asymmetry of strain gages in these two channels. Obviously, the sensitivity of the PEEK sensor is much higher than that of the metallic sensor.

E. CROSSTALK

It can be seen from Fig. 8 that, due to the influence of loading cap, torque applied to the PEEK sensor in Z direction (*i.e. Tz*) has a larger crosstalk towards *Fz* and *Tx* than other components. The crosstalk occurring may be due to misalignments

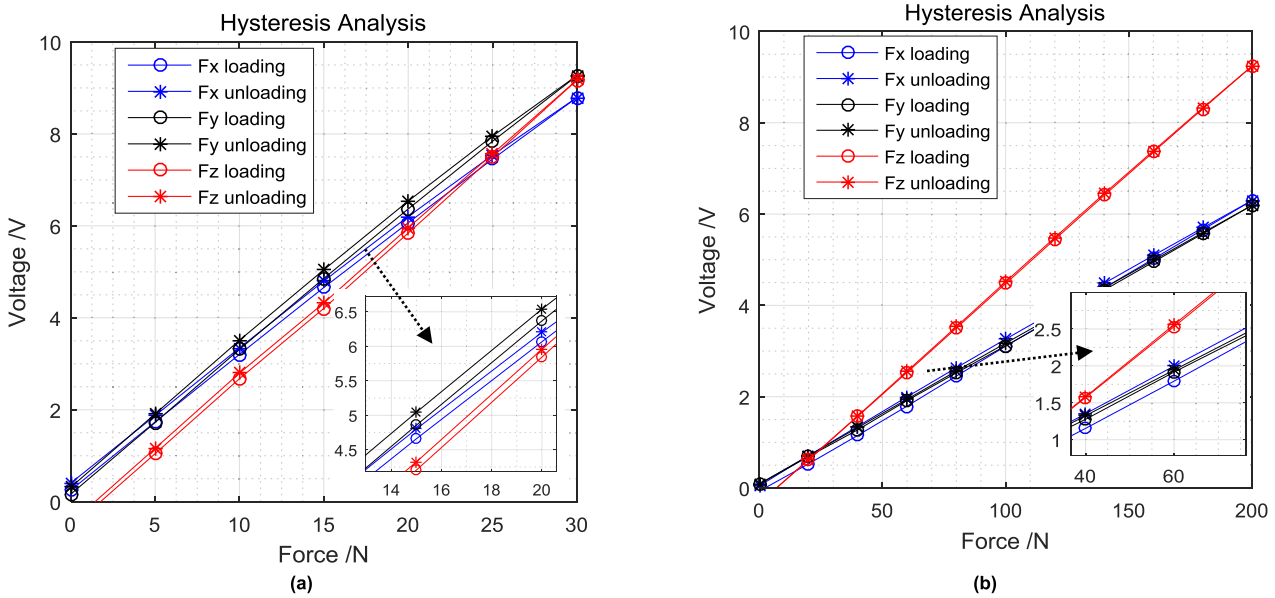

FIGURE 10. The comparison of hysteresis of the two F/T sensors: (a) PEEK sensor; (b) metallic sensor.

TABLE 9. Main performance parameters of the PEEK sensor.

	Measurement range		Linearity		repeatability		Hysteresis		Sensitivity		Crosstalk error
	PEEK	metallic	PEEK	metallic	PEEK	metallic	PEEK	metallic	PEEK	metallic	PEEK
Fx	±30N	±200N	≤1%	≤0.5%	±1.53	±1.96	±1.75	±1.97	2.37	0.11	4.28%
Fy	±30N	±200N	≤1%	≤0.5%	±1.85	±1.92	±1.88	±1.26	2.46	0.11	4.35%
Fz	±30N	±200N	≤0.5%	≤0.5%	±1.29	±0.41	±1.33	±0.56	2.5	0.17	7.95%
Tx	±0.3Nm	±2Nm	≤0.5%	≤0.5%	±1.06	±1.35	±1.2	±1.59	0.19	0.013	7.86%
Ty	±0.3Nm	±2Nm	≤0.5%	≤0.5%	±1.13	±0.88	±1.31	±1.62	0.19	0.013	5.95%
Tz	±0.5Nm	±4Nm	≤1%	≤1%	±2.21	±1.5	±1.92	±1.99	0.038	0.00295	3.24%

during strain gages bonding or stems from calibration direction deviation [33]. It can be drawn from the above figures that the output voltages due to the applied forces and torques can be summarized as (13), shown at the bottom of this page, where the unit of force is 'N', torque is 'Nmm', and output voltage is 'V'. The off-diagonal components represent the crosstalk, and the main-diagonal components represent the sensitivity. The crosstalk error is defined as (14).

$$E_i = \sqrt{\frac{\sum_{j=1,j\neq i}^{6} \left|y_{ij(\max)}\right|^2}{\left|y_{i(F.S.)}\right|^2}} \tag{14}$$

where $y_{i(F.S.)}$ denotes full scale value of the applied force/torque in i direction; $y_{ij(\max)}$ represents the maximum force/torque measured in i direction when there is an acting force/torque only in j direction; $i(= 1, 2, \ldots, 6)$ denotes one of the six directions of six-axis F/T sensor. Consequently the crosstalk errors of the PEEK sensor obtained are as shown in the last column of Table 9. It can be seen that the crosstalk errors of the PEEK sensor in Fz and Tx directions are large up to about 7.9%, and therefore decoupling in the two directions need to be strengthened. And Table 9 summarizes the cha racteristics of the PEEK sensor as well as the performance comparison with the metallic sensor. It is evident from Table 9 that the linearity, repeatability, and hysteresis of the PEEK sensor

$$\begin{bmatrix} F_x \\ F_y \\ F_z \\ T_x \\ T_y \\ T_z \end{bmatrix} = \begin{bmatrix} 3.29 & -0.033 & -0.032 & 0.128 & -0.066 & -0.044 \\ -0.034 & 3.23 & 0.028 & 0.062 & -0.125 & 0.056 \\ 0.016 & 0.006 & 3.19 & -0.092 & 0.021 & -0.252 \\ 0.268 & -1.57 & -2.12 & 33.46 & -0.205 & -1.63 \\ 1.66 & 0.37 & -1.31 & 0.16 & 33.38 & 0.057 \\ 0.36 & 1.21 & 1.91 & 1.87 & 2.1 & 56.82 \end{bmatrix} \begin{bmatrix} U_{Fx} \\ U_{Fy} \\ U_{Fz} \\ U_{Tx} \\ U_{Ty} \\ U_{Tz} \end{bmatrix} \tag{13}$$

are simillar to the metallic sensor, whereas the sensitivity is tens of times different.

VI. DYNAMIC PERFORMANCES ANALYSIS AND COMPARISON

The step-response method is used to calibrate the two six-axis F/T sensors dynamically. The dynamic calibration experiment was carried out by cutting the fishing line hanging the weight to construct the negative step excitation [34]. One end of the fishing line is hung on the calibration pillar, the other end is suspended the weight through a pulley. The fishing line is cut off at a given time, thus a negative step excitation is applied to the sensor. The step responses in the X direction are plotted in Fig. 11. It is observed that the response time of the PEEK sensor is 46ms, which is four times that of the metallic sensor. As the results of the FEA, the natural frequency of the PEEK sensor is much lower than that of the metallic sensor, and hence the PEEK sensor is only suitable for lower frequency signal measurement (below 200Hz).

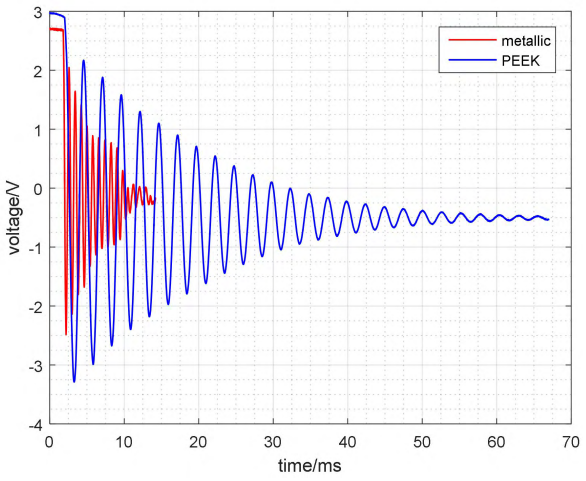

FIGURE 11. The step responses of the two sensors in Fx direction.

VII. CONCLUSIONS

Owing to the excellent mechanical properties of PEEK, it can be used to fabricate elastic beam of a six-axis F/T sensor. Various performance indices of the PEEK sensor are obtained via FEA and calibration experiments, and compared with the metallic sensor. It is observed that the linearity, repeatability and hysteresis of the PEEK sensor are simillar to the metallic sensor, whereas the sensitivity is tens of times that of the metallic sensor. Crosstalk between the dominant channel and other channels is a little large, in which the interference of Tz to Fz and Tx can reach 7.95%. However, the problem of crosstalk can be solved by appropriate decoupling methods. In addition, the dynamic response time in Fx channel is 46ms, nearly four times that of the metallic sensor. Therefore, PEEK can be used to fabricate highly sensitive six-axis F/T sensor, but this kind of sensor is not suitable for dynamic measurement beyond 200Hz. Because of its light weight and high sensitivity, the PEEK sensor is very suitable for aerospace and medical fields. PEEK is more sensitive to temperature than aluminum alloy; hence the temperature drift performance of the PEEK sensor will be studied in the near future.

REFERENCES

[1] G. Hirzinger, B. Brunner, J. Dietrich, and J. Heindl, "Sensor-based space robotics-ROTEX and its telerobotic features," *IEEE Trans. Robot. Autom.*, vol. 9, no. 5, pp. 649–663, Oct. 1993.
[2] L.-P. Chao and C.-Y. Yin, "The six-component force sensor for measuring the loading of the feet in locomotion," *Mater. Design*, vol. 20, pp. 237–244, Oct. 1999.
[3] Q. K. Liang, D. Zhang, G. Coppola, and J. X. Mao, "Design and analysis of a sensor system for cutting force measurement in machining processes," *Sensors*, vol. 16, no. 1, p. 70, Jan. 2016.
[4] U. Zuperl, T. Irgolic, and F. Cus, "Surface roughness monitoring in cutting force control system," *Proc. Manuf. Syst.*, vol. 10, no. 2, pp. 59–64, 2015.
[5] G.-S. Kim, H.-J. Shin, and J. Yoon, "Development of 6-axis force/moment sensor for a humanoid robot's intelligent foot," in *Proc. IEEE Sensors*, Oct. 2007, pp. 217–220.
[6] RUAG Aerospace Defence Technology, (2005). *Strain Gauge Balances for Wind Tunnel Measurements*. [Online]. Available: http://www.ruag.com
[7] H. Wu, X. D. Ma, and K. Qian, "Development of robot assembly system based on real-time force control," *Ind. Control Comput.*, vol. 30, pp. 44–46, 2017.
[8] L. J. Zhang, R. Q. Hu, and W. M. Yi, "Research on force sensing for the end-load of industrial robot based on a 6-axis force/torque sensor," *Acta Automatica Sinica*, vol. 43, no. 7, pp. 439–447, 2017.
[9] F. Ballo, M. Gobbi, G. Mastinu, and G. Previati, "Advances in force and moments measurements by an innovative six-axis load cell," *Exp. Mech.*, vol. 54, no. 4, pp. 571–592, Apr. 2014.
[10] G. Lin, H. Pang, W. Zhang, D. Wang, and L. Feng, "A self-decoupled three-axis force sensor for measuring the wheel force," *Proc. Inst. Mech. Eng. D, J. Auto. Eng.*, vol. 228, pp. 319–334, Feb. 2014.
[11] Y. Noh, J. Bimbo, S. Sareh, H. Wurdemann, J. Fraś, D. S. Chathuranga, H. Liu, J. Housden, K. Althoefer, and K. Rhode, "Multi-axis force/torque sensor based on simply-supported beam and optoelectronics," *Sensors*, vol. 16, no. 11, p. 1936, Nov. 2016.
[12] A. Song, J. Wu, G. Qin, and W. Huang, "A novel self-decoupled four degree-of-freedom wrist force/torque sensor," *Measurement*, vol. 40, nos. 9–10, pp. 883–891, Nov-Dec. 2007.
[13] J. W. Guggenheim, L. P. Jentoft, Y. Tenzer, and R. D. Howe, "Robust and inexpensive six-axis force-torque sensors using MEMS barometers," *IEEE/ASME Trans. Mechatronics*, vol. 22, no. 2, pp. 838–844, Apr. 2017.
[14] U. Kim, D.-H. Lee, Y. B. Kim, D.-Y. Seok, and H. R. Choi, "A novel six-axis force/torque sensor for robotic applications," *IEEE/ASME Trans. Mechatronics*, vol. 22, no. 3, pp. 1381–1391, Jun. 2017.
[15] W. Zhang, K. B. Lua, V. T. Truong, K. A. Senthil, T. T. Lim, K. S. Yeo, and G. Zhou, "Design and characterization of a novel T-shaped multi-axis Piezoresistive force/moment sensor," *IEEE Sensors J.*, vol. 16, no. 11, pp. 4198–4210, Jun. 2016.
[16] J. T. Yao, Y. L. Hou, H. Wang, and Y. Zhao, "Isotropic design of Stewart platform-based force sensor," in *Proc. ICIRA*, Wuhan, China, Oct. 2008, pp. 723–732.
[17] Y. Z. Zhao, C. Zhang, D. Zhang, Z. Shi, and T. Zhao, "Mathematical model and calibration experiment of a large measurement range flexible joints 6-UPUR six-axis force sensor," *Sensors*, vol. 16, no. 8, p. 1271, Aug. 2016.
[18] Q. Liang, D. Zhang, Q. Song, Y. Ge, H. Cao, and Y. Ge, "Design and fabrication of a six-dimensional wrist force/torque sensor based on E-type membranes compared to cross beams," *Measurement*, vol. 43, no. 10, pp. 1702–1719, Dec. 2010.
[19] A. Cherubini, R. Passama, A. Crosnier, A. Lasnier, and P. Fraisse, "Collaborative manufacturing with physical human–robot interaction," *Robot. Comput. Integr. Manuf.*, vol. 40, pp. 1–13, Aug. 2016.
[20] J. F. Shi, D. Q. Wang, and F. L. Yan, "Research of the direct teaching of industrial robots based on active compliance control," *Modular Mach. Tool Autom. Manuf. Technique*, no. 12, pp. 66–69, 2017.
[21] [Online]. Available: http://www.zypeek.cn/english/
[22] A. Song and L. Fu, "Multi-dimensional force sensor for haptic interaction: A review," *Virtual Reality Intell. Hardw.*, vol. 1, no. 2, pp. 121–135, Jan. 2019.

[23] T. E. Attwood, P. C. Dawson, J. L. Freeman, L. R. J. Hoy, J. B. Rose, and P. A. Staniland, "Synthesis and properties of polyaryletherketones," *Polymer*, vol. 22, no. 8, pp. 103–1096, Aug. 1981.
[24] V. L. Rao, "Polyether ketones," *J. Macromolecular Sci. C, Polymer Rev.*, vol. 35, no. 4, pp. 661–712, Nov. 1995.
[25] Victrex, Plc. (2011). *Product Data Sheet, Victrex PEEK*. Available: [Online]. Available: http://www.victrex.com/
[26] A. M. Díez-Pascual, M. Naffakh, C. Marco, G. Ellis, and M. A. Gómez-Fatou, "High-performance nanocomposites based on polyetherketones," *Prog. Mater. Sci.*, vol. 57, no. 7, pp. 1106–1190, Sep. 2012.
[27] V. Balaji, A. N. Tiwari, and R. K. Goyal, "Study on high-performance poly(etheretherketone)/Si_3N_4 nanocomposites: New electronic substrate materials," *Polym. Eng. Sci.*, vol. 51, no. 3, pp. 509–517, Mar. 2011.
[28] W. M. Doyle, "Aluminum alloys: Structure and properties," *Metal Sci.*, vol. 35, no. 11, p. 408, 1976.
[29] S. P. Timoshenko, "On the transverse vibrations of bars of uniform cross-section," *London, Edinburgh, Dublin Philos. Mag. J. Sci.*, vol. 43, pp. 125–131, Jan. 1922.
[30] R. G. Budynas, "Topics from advanced mechanics of materials," in *Advanced Strength and Applied Stress Analysis*, 2nd ed. New York, NY, USA: McGraw-Hill, 2001, pp. 272–302.
[31] J. Ma and A. Song, "Fast estimation of strains for cross-beams six-axis force/torque sensors by mechanical modeling," *Sensors*, vol. 13, no. 5, pp. 6669–6686, 2013.
[32] W. Ke, F. Du, and X. Zhang, "Algorithm and experiments of six-dimensional force/torque dynamic measurements based on a Stewart platform," *Chin. J. Aeronaut.*, vol. 29, no. 6, pp. 1840–1851, Dec. 2016.
[33] L. Y. Fu and A. G. Song, "Error analysis of six-axis force/torque sensor's static calibration system," *Acta Metrologica Sinica*, vol. 40, no. 2, pp. 295–299, 2019.
[34] L. Fu and A. Song, "An optimized BP neural network based on genetic algorithm for static decoupling of a six-axis force/torque sensor," in *Proc. IOP Conf. Ser. Mater. Sci. Eng.*, Taiwan, China, vol. 311, Feb. 2018, Art. no. 012002.

LIYUE FU received the M.S. degree in biomedical engineering from Shandong University, Jinan, China, in 2009. She is currently pursuing the Ph.D. degree in instrument science and technology with Southeast University, China. She focuses her work on robot sensing and control technology.

AIGUO SONG received the B.S. degree in automatic control, the M.S. degree in measurement and control from the Nanjing University of Aeronautics and Astronautics, Nanjing, China, in 1990 and 1993, respectively, and the Ph.D. degree in measurement and control from Southeast University, Nanjing, in 1996. From 1996 to 1998, he was an Associate Researcher with the Intelligent Information Processing Laboratory, Southeast University. From 1998 to 2000, he was an Associate Professor with the Department of Instrument Science and Engineering, Southeast University, where he was the Director of the Robot Sensor and Control Laboratory, from 2000 to 2003. From April 2003 to April 2004, he was a Visiting Scientist with the Laboratory for Intelligent Mechanical Systems, Northwestern University, Evanston, IL, USA. He is currently a Professor with the Department of Instrument Science and Engineering, Southeast University. His research interests include haptic display, robot tactile sensor, and tele-rehabilitation robot. He is a member of the Chinese Instrument and Control Association.

DAPENG CHEN received the B.S. degree in electrical engineering and automation from the Anhui University of Science and Technology, Huainan, China, in 2011. He is currently pursuing the Ph.D. degree in instrument science and technology with the Robotic Sensor and Control Laboratory, Southeast University. He visited the Intelligent, Multimedia, and Interactive Systems Laboratory, University of North Carolina at Charlotte, from 2016 to 2017. His research interests include haptic display, haptic device, and human–computer interaction.